ELSEVIER

Contents lists available at ScienceDirect

Journal of Fluids and Structures

journal homepage: www.elsevier.com/locate/ifs



Vibration of a thin panel exposed to ramp-induced shock-boundary layer interaction at Mach 2



Marc A. Eitner*, Yoo-Jin Ahn, Mustafa N. Musta, Noel T. Clemens, Jayant Sirohi

The University of Texas at Austin, Department of Aerospace Engineering and Engineering Mechanics, 2617 Wichita Street. Austin. 78712. TX. USA

ARTICLE INFO

Article history: Received 22 November 2022 Received in revised form 1 March 2023 Accepted 13 April 2023 Available online 2 May 2023

Keywords: SBLI Panel vibration Supersonic Pressure sensitive paint Digital image correlation

ABSTRACT

Flight vehicles that operate in the supersonic regime can be subject to adverse fluidstructure interactions due to their lightweight design. The presence of geometric obstructions such as control surfaces or fins can induce shocks that can interact with the boundary layer, leading to flow separation. This work investigates experimentally the interaction between a compliant panel in a Mach 2 flow under a compression rampinduced shock-wave/boundary-layer interaction (SBLI). Thin brass panels of different thickness are investigated in a wind tunnel. Tests are performed both with and without a 20° compression ramp installed. This direct comparison allows characterization of the effect of the SBLI on the system dynamics. High-speed stereoscopic digital image correlation (DIC) and fast-response pressure sensitive paint (PSP) are used to obtain simultaneous measurements of full field deformation and surface pressure of the panels. The panel vibration is dominated by the first bending mode. Despite the forcing of the separation shock foot, the presence of the SBLI does not significantly modify the operational deflection shape, frequency, and amplitude of the dominant vibration mode, beyond what is observed for the no-SBLI case. On the other hand, analysis of the shock foot motion shows that the shock primarily oscillates at the first natural frequency of the panel. This leads to the conclusion that the shock foot oscillation is driven by the panel vibration in a one-way coupling mechanism. The SBLI does modify the higher modes, which is likely due to localized forcing by the separation shock foot. Full-field surface pressure predictions are made using first order piston theory. Results show that the fluid-structure interaction is dominated by the large region of attached flow upstream of the shock foot.

© 2023 Elsevier Ltd. All rights reserved.

1. Introduction

High-speed vehicles operating in supersonic flow regimes are subjected to a variety of loads arising from effects such as aero-thermal heating, compressible flow phenomena and turbulence-induced broadband excitation. The interaction of high-speed flows and structural dynamics is complex, and requires significant effort in numerical modeling as well as experimental measurements (Frendi, 1997; Mei et al., 1999; Casper et al., 2019; Dowell, 1970; Freydin and Dowell, 2021). The interaction becomes even more complex when structures are forced by the presence of shock wave/boundary layer interactions (SBLI), which can exhibit large-scale boundary layer separation and low-frequency unsteadiness that can couple to the structural dynamics. Such interactions have been the subject of several experimental and numerical

E-mail address: marceitner@utexas.edu (M.A. Eitner).

^{*} Corresponding author.

studies (Maestrello and Linden, 1971; Willems et al., 2013; Brouwer et al., 2017; Varigonda and Narayanaswamy, 2019; Tan et al., 2019; Spottswood et al., 2019; Neet and Austin, 2020; Schöneich et al., 2021) that aim to better understand the underlying physical relations with the goal of creating improved numerical modeling techniques.

One type of SBLI that has been extensively studied in the context of flow-structure interaction, is the reflected shock interaction. In such interactions, an oblique shock is generated in the upstream region on the wall opposite to the panel, which then impinges on it. The physical phenomena relevant to this type of interaction are as follows. The boundary layer over the panel is typically turbulent at high enough Reynolds numbers. The turbulence acts as a spatially uncorrelated, broadband excitation that forces all panel modes to vibrate, though the first mode typically has the largest amplitude. The impinging shock wave interacts with the boundary layer and creates a complicated pattern of compression and expansion waves. For sufficiently strong shocks, the flow will separate and reattach further downstream, creating a flow separation bubble. The mean static wall pressure acts as a static forcing function on the panel. The motion of the shock foot and the associated surface pressure near it is dominated by unsteadiness. It occurs at low frequencies, near Strouhal numbers of $St = fL_s/U_\infty \approx O(0.01)$, where L_s is the size of the separation bubble and U_∞ is the free stream velocity. This unsteadiness is locally constrained to a small intermittent region and the resulting pressure fluctuations can excite only specific panel modes (Eitner et al., 2022).

Spottswood et al. (2012, 2019) studied a reflected shock interaction over a fully clamped steel panel in a multi-year experimental campaign. Results showed especially the benefit of utilizing full-field diagnostic techniques such as digital image correlation (DIC) and pressure sensitive paint (PSP), as well as the importance that heating of the flow can have on the panel response. Varigonda et al. (2021) performed a detailed analysis of the surface pressure fields for PSP and quantified the effect of panel stiffness changes at different flow conditions. They found that localized forcing resulting from the SBLI played a significant role in the panel vibration. Particle image velocimetry (PIV) and steady PSP was used by Tripathi et al. (2021) along with discrete displacement measurements. They identified significant influence of cavity pressure and shock impingement locations on the separation lengths. Tan et al. (2019) identified separation length from oil flow tests as a result of panel curvature and found that curvature results in shorter separation lengths. Neet and Austin (2020) experimented on curved panels and used Schlieren imaging and PSP for their study in a Mach 4 Ludwieg tube. They also found an increase of separation length with large panel deformation. Additional experimental and numerical investigations have been made on panels with different boundary conditions, such as clamped-free-clamped-free (Willems et al., 2013; Vasconcelos et al., 2021) or clamped-free-free-free (Thayer et al., 2022; Currao et al., 2017).

Another type of SBLI-induced FSI is that induced by the presence of a compression ramp. The compression-ramp and reflected shock interactions exhibit significant similarities regarding their shock and separated flow structure, and unsteadiness (Babinsky and Harvey, 2014). The problem of ramp-induced SBLI for example was investigated by Schöneich et al. (2021) and Whalen et al. (2020), who analyzed a system with a compliant panel inserted into the ramp. They investigated Mach 6 flow over the ramp with an angle variable between 10°–35°. They identified aerothermal heating as the primary reason for changes in panel stiffness. They further identified localized forcing from the SBLI to have a large influence on panel vibration amplitude.

Within the current body of literature, there is currently no consensus on how the presence of SBLI affects the dynamics of the panel vibration. Simplified theoretical relations exist that describe the coupling between supersonic flow and panel vibration, such as piston theory. Such relations however do not exist for the more complex case where SBLI occurs and disturbs the flow. This study aims to experimentally characterize how the dynamics of the panel vibrations change in the presence of supersonic flow and SBLI.

In the present work, a set of thin brass panels of length 121.9 mm, width 63.5 mm, and different thicknesses (h = 0.508 mm, 0.406 mm, 0.305 mm, and 0.254 mm) are inserted into a rectangular cutout in the floor of a Mach 2 wind tunnel. A 20° compression ramp (25 mm tall) is located immediately downstream of the panel insert. This system creates an SBLI on the panel. To evaluate the effect of the SBLI on the panel dynamics, each panel is tested twice, once without the ramp and then with the ramp. This allows isolation of the system changes that result from the presence of the SBLI. Apart from the presence of the ramp, all test parameters remain unchanged between the two consecutive test runs. Using high-speed DIC, the out-of-plane panel deformation is measured. A system identification technique known as complexity pursuit (CP) is utilized to obtain the operational deflection shapes of the panel. The flow-facing side of the panel is painted with pressure sensitive paint and recorded at 50 kHz, resulting in measurements of the full-field surface pressure. Deformation and pressure are measured synchronously, which allows for the computation of the correlation between the two. Piston theory is then used to predict surface pressure fields from the deformation of the panel.

The present study uses lessons learned from previous work performed in the field, especially with respect to measurement techniques and fabrication of test articles. This study adds novelty to the field by utilizing new algorithms (e.g. Complexity Pursuit for system identification), a parametric approach (multiple panel thicknesses), and direct comparison between test cases without and with an SBLI. Before the experiments are discussed, an introduction to panel vibration and SBLI are provided in Section 2. In Section 3, the setup of the experiments is described along with details regarding the measurement techniques. Section 4 contains the results of experiments performed to characterize the dynamic behavior of the panels in different conditions (no flow, flow without ramp, flow with ramp). The last section summarizes all insights gained from this study and discusses remaining open questions.

2. Physical principles

This section has the purpose to introduce the reader to some fundamental theory that describes the behavior of thin panels in the presence of supersonic flow. Many relations cannot easily be discussed with simple equations and thus a numerical model is used to demonstrate the structural and aerodynamic characteristics of thin panels in supersonic flow. For this reason, an extended version of the aerothermoelastic model by Freydin and Dowell (2021) was implemented in an in-house MATLAB code. The model is used to illustrate three important effects, namely the coupling between aerodynamics and structural dynamics, the mode coalescence leading to panel flutter and the effect of in-plane tension on bending stiffness.

2.1. Numerical model

The model is derived using the Rayleigh–Ritz method, which uses combinations of one-dimensional mode shapes of beams that are clamped on both sides as basis functions to describe the bending deformation of the panel. The model is clamped on all sides but has variable in-plane stiffness along the edges. In-plane inertia is neglected and a viscous damping term is added for the out-of-plane bending deformation. The resulting system of differential equations for the bending deformation w is:

$$M_{nk}\ddot{w}_k + C_{nk}\dot{w}_k + A_{\dot{w}_{nk}}\dot{w}_k + D_{nkrs}^{(2)}w_kw_rw_s + A_{w_{kn}}w_k + G_{nk}^{(2)}w_k + Q_n = 0$$
(1)

The indices/subscripts indicate a specific mode and repeated indices imply summation. The second-order tensors represent the inertia (M), the linear structural stiffness $G^{(2)}$, viscous damping C, aerodynamic stiffness A_w and aerodynamic damping $A_{\dot{w}}$. Q represents a forcing term and $D^{(2)}$ contains all non-linear structural stiffness terms. All notations are identical to those used by Freydin and Dowell in the original paper (Freydin and Dowell, 2021) and are further discussed below.

2.1.1. Structural model

The model is based on isotropic linear elastic material behavior, includes the effect of thermal stresses, and is valid for thin plates without initial curvature. The panel bending was described using 32 basis functions. In addition, 101 basis functions are used to describe the in-plane deformation. The in-plane degrees of freedom are then expressed as a function of the bending deformation and thus only Eq. (1) needs to be solved. The matrices M, $G^{(2)}$ and C describe the inertia, structural damping, and linear stiffness respectively. These three terms describe the dynamic behavior of a panel undergoing small motion w < h. The fourth-order tensor $D^{(2)}$ describes the nonlinear bending stiffness of the panel. This term becomes important when the deformation is on the order of the panel thickness. The terms $A_{\tilde{w}}$ and $A_{\tilde{w}}$ are the aerodynamic damping and stiffness terms; in this analysis, they are derived from first-order piston theory. The final term O is a static loading term that describes a pressure difference between the top and bottom sides of the panel.

2.1.2. Aerodynamic model

The two linear aerodynamic terms $A_{\bar{w}}$ and A_w are derived from first-order piston theory, which states that fluid flowing over a moving surface at freestream Mach number M_{∞} , density ρ_{∞} and velocity U_{∞} experiences a local pressure change $p-p_{\infty}$:

$$p - p_{\infty} = \frac{\rho_{\infty} U_{\infty}}{M_{\infty}} \left(\frac{\partial w}{\partial t} + U_{\infty} \frac{\partial w}{\partial x} \right) \tag{2}$$

The pressure change comes from two terms, the vertical velocity of the panel and the streamwise slope (or wall angle). This form of the piston theory is generally applicable at high Mach numbers and when the Mach number times the deflection/chord ratio is much smaller than unity. The first term in Eq. (2) creates the aerodynamic damping. The second term is responsible for the aerodynamic stiffness. The linear stiffness of the system is determined by the sum of the structural stiffness $G^{(2)}$ and aerodynamic stiffness A_w . As the scaling factor $\lambda = \frac{\rho_\infty U_\infty^2}{M_\infty} = \frac{2q_\infty}{M_\infty} = \gamma p_\infty M_\infty$ grows (q_∞ is the dynamic pressure, γ is the isentropic exponent, p_∞ is the freestream static pressure), the influence of the aerodynamic stiffness increases and modifies the characteristics of the system, i.e. its natural frequencies and mode shapes. To show the influence of aerodynamic stiffness, the first two natural frequencies of the panel are calculated for different values of λ and shown in Fig. 1. The frequencies change and coalesce at some critical value of λ , after which there is only one mode that is typically unstable (the effective damping for that mode is negative). This instability is known as coupled mode flutter and is typical for the combination of Mach number and panel aspect ratio discussed in this work (Dowell, 1974). The mode shapes for the first and second mode are also shown in Fig. 1. At $\lambda = 0$ the mode shapes are perfectly symmetric, but as the dynamic pressure q_∞ is increased and λ grows, the peaks of the modes (i.e. the antinodes) shift to the right (downstream) due to the coupling of the aerodynamic terms. In the flutter state, there is only one mode that has a shape that looks like a combination of the first and second mode. Since these mode shapes no longer represent the pure linear modes from the free response equations, they are more commonly referred to as operational deflection shapes (ODS). This more general term is used for the remainder of this work.

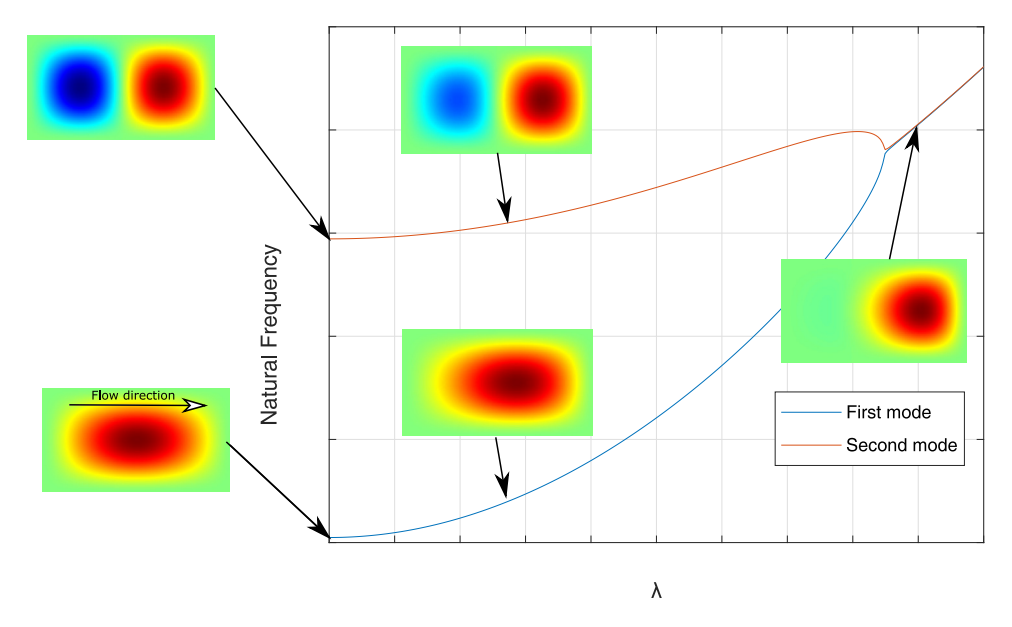


Fig. 1. Influence of aerodynamic stiffness on natural frequencies and operational deflection shapes.

2.2. Effect of in-plane tension

Both the linear and non-linear bending stiffness terms in Eq. (1) increase in the presence of in-plane stretching. In-plane stretching can occur as a result of three effects: external tensile forces, temperature gradients, and large bending deformation.

- 1. External tensile forces are generally not wanted but can occur when the model is installed and bolted into a fixture, resulting in in-plane displacements at the boundaries. They can also be remnants of the fabrication process, such as when a slightly curved panel is stretched and bonded to a fixed support. When the external forces act in compression (N < 0), the bending stiffness decreases and so do the natural frequencies.
- 2. Temperature gradients typically occur in wind tunnel tests, where the fluid either cools or heats the panel, depending on its recovery temperature. The panel typically cools or heats faster than its support, leading to thermal gradients that can have large effects on the panel frequencies. In the case where the panel is colder than its support $(\Delta T < 0)$, the temperature gradients increase the bending stiffness, whereas in the opposite case the bending stiffness is reduced for a hot panel. A detailed discussion of this effect can be found in Freydin and Dowell (2021).
- 3. Large bending deformations on the order of the panel thickness also lead to in-plane stretching. These large deformations commonly occur due to static pressure differences $\Delta P = p_{cavity} p_{\infty}$ across the panel. The term p_{cavity} refers to the static pressure on the side of the panel that is not exposed to the flow and in most experimental setups is enclosed by a cavity.

The effect of external in-plane forces, temperature gradients, and large bending deformations are summarized in Fig. 2. The numerical model was used to compute the natural frequency of the first mode for a panel subject to these three effects. The figure is mainly illustrative and intended to show certain trends. The frequency increase depends on many other parameters, such as panel thickness h and in-plane boundary stiffness K. This specific plot is somewhat representative of the panels used in this study, though it is not an updated model that exactly matches the experimental results. The range of values simulated is $\Delta P = \pm 3.5$ kPa, $\Delta T = \pm 0.3$ K and $N/K = \pm 10$ μ m. All values are normalized by their maximum value on the horizontal axis of the plot.

Temperature gradients and external in-plane forces affect the natural frequency in a similar way and can lead to an increase and decrease in stiffness. The large deformation was computed by applying a steady pressure difference ΔP across the panel. The direction of deformation has no effect on the stiffening effect, provided that the panel is perfectly flat initially. A slight initial curvature of the panel results in behavior that is also slightly dependent on the direction of the applied pressure load. The minimum frequency value will no longer occur at $\Delta P = 0$ but rather at some small pressure offset. Such an effect can be seen later in the experimental data, but cannot be simulated with the flat plate model used here.

2.3. Nature of the surface pressure

The physical principles discussed so far apply to a panel subject to an attached supersonic flow. The surface pressure changes significantly in the presence of an SBLI, by changing the static pressure distribution and introducing

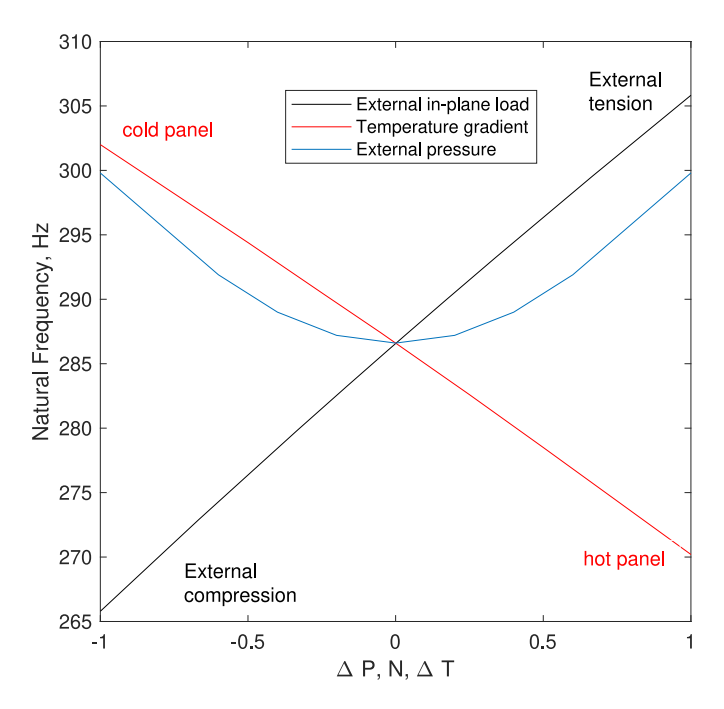


Fig. 2. Causes of in-plane tension and their effects on natural frequency of first bending mode.

low-frequency shock unsteadiness. To show the behavior of the surface pressure, measurement data is discussed here that was taken in the Mach 2 wind tunnel at The University of Texas at Austin, under the same conditions as for all other data sets discussed in this paper.

The surface pressure field was measured on a rigid (25 mm thick) panel just upstream of the 20° compression ramp. At each location on the panel, the time history of the normalized pressure p/p_{∞} was extracted and its mean (Fig. 3(a)) and standard deviation (Fig. 3(b)) were computed. Fig. 3(a) clearly shows the region of increased pressure downstream of the shock foot around x = 100 mm. Fig. 3(b) shows the intermittent region of the separation shock foot, which leads to a thin band of large pressure fluctuations, with a streamwise extent of approximately one boundary layer thickness. The position of the shock foot was estimated from low-pass filtered and down-sampled PSP data in each frame and used to show time-histories and spectra in the following plots. The computation is based on finding the streamwise location of surface pressure rise, which indicates the shock foot position. A detailed description of how the shock foot motion was computed is later given in Section 4.5, when the relation between panel vibration and shock motion is discussed. Shown in Fig. 3(c) is the time history of the shock foot motion, extracted near the centerline at y = -11 mm. (The rigid panel insert featured seven small holes for pressure transducers along the centerline, that were used to calibrate the PSP and therefore surface pressure data could not be extracted along the centerline.) The shock foot motion shows significant unsteadiness with a mean value of around 100 mm. A comparison of the standard deviation of the pressure (at y =-11 mm) with the range of motion of the shock foot is provided in Fig. 3(d). The region of large pressure fluctuations near x = 100 mm can be explained by the shock unsteadiness. A PSD of the shock foot motion is shown in Fig. 3(e), along with a zoomed-in time history. The flow separation occurs not exactly at the beginning of the pressure rise, but rather slightly downstream of that, see e.g. Dolling and Or (1985). Based on those reference values, we estimate that the actual flow separation occurs closer to around x = 110 mm. This is 17 mm upstream of the compression ramp, or 1.7 δ_{99} . If the shock foot motion is plotted in a different way, the dominant low-frequency unsteadiness of the SBLI becomes visible. Fig. 3(f) shows (in orange) a spectrum of the shock foot motion (power spectral density premultiplied with frequency and normalized by its variance). The plot shows that low frequencies below 1000 Hz dominate the spectrum. This is also evident in the spectrum of the surface pressure (local PSP data from the intermittent region near the centerline at x =92 mm), shown in blue in the same plot. For further details on the SBLI in this setup, the interested reader is referred to the work by Ahn et al. (2022) in which the flow field was investigated using particle image velocimetry.

3. Experimental setup and measurement techniques

This section discusses the wind tunnel test facility as well as the experimental setup and measurement techniques used. The design and fabrication process of the test articles is also elaborated.

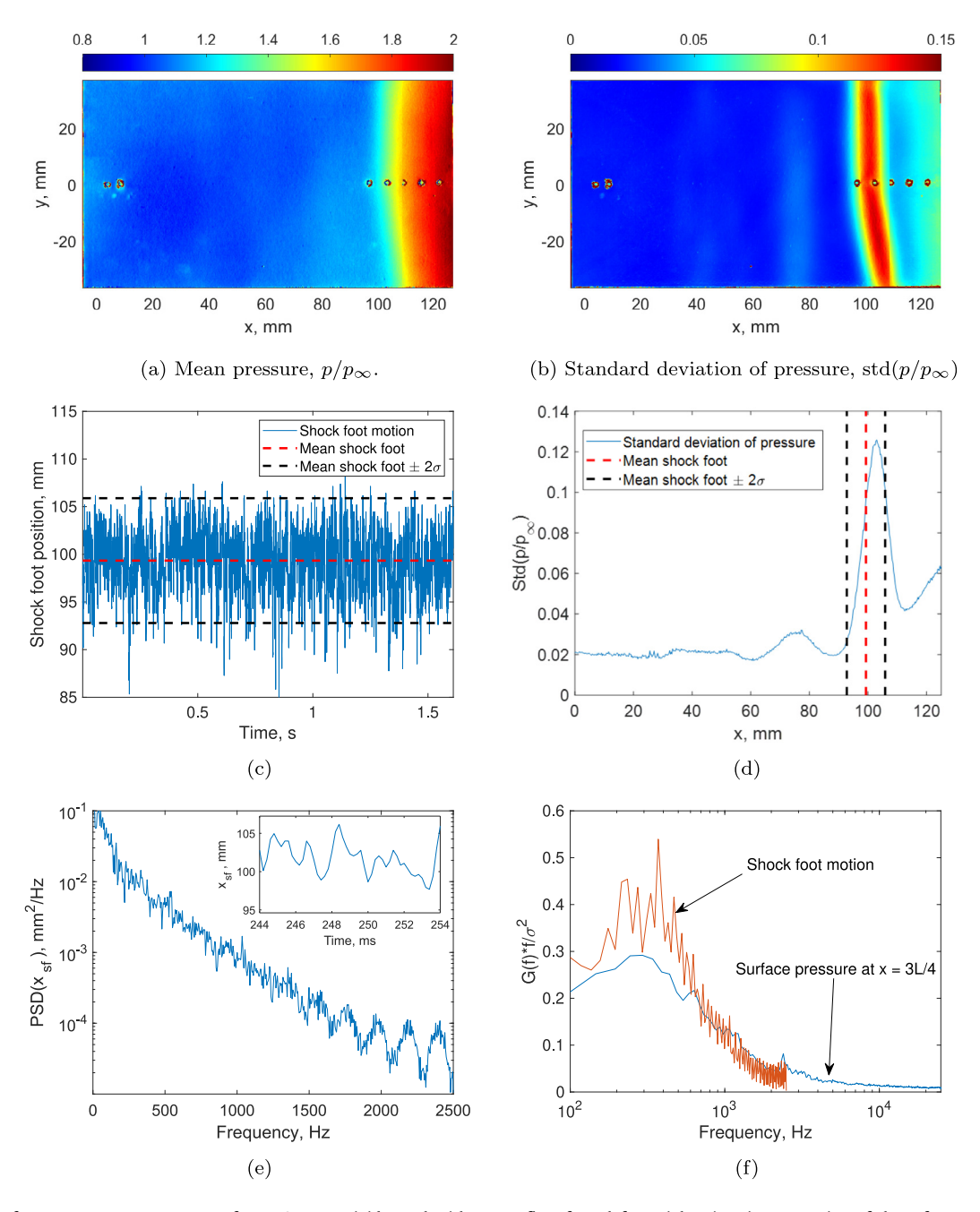


Fig. 3. Surface pressure measurements from PSP on a rigid panel with ramp; flow from left to right;. (For interpretation of the references to color in this figure legend, the reader is referred to the web version of this article.)

Table 1Wind tunnel flow parameters in test section.

Velocity U_{∞} [m/s]	Stagnation pressure p_0 [kPa]	Stagnation temperature T_0 [K]	Boundary layer thickness δ_{99} [mm]	Re_{∞} [m ⁻¹]
514 ± 4	345 ± 5	285 ± 3	10.3 ± 1.4	1×10^8

3.1. Mach 2 wind tunnel

All experiments were performed in the Mach 2 blow-down wind tunnel of The University of Texas at Austin. Each tunnel run can last for up to 30 s. The cross-section of the rectangular test section has a width and height of 152 mm and 157 mm respectively. The flow conditions are listed in Table 1. Flow velocity and boundary layer thickness were obtained

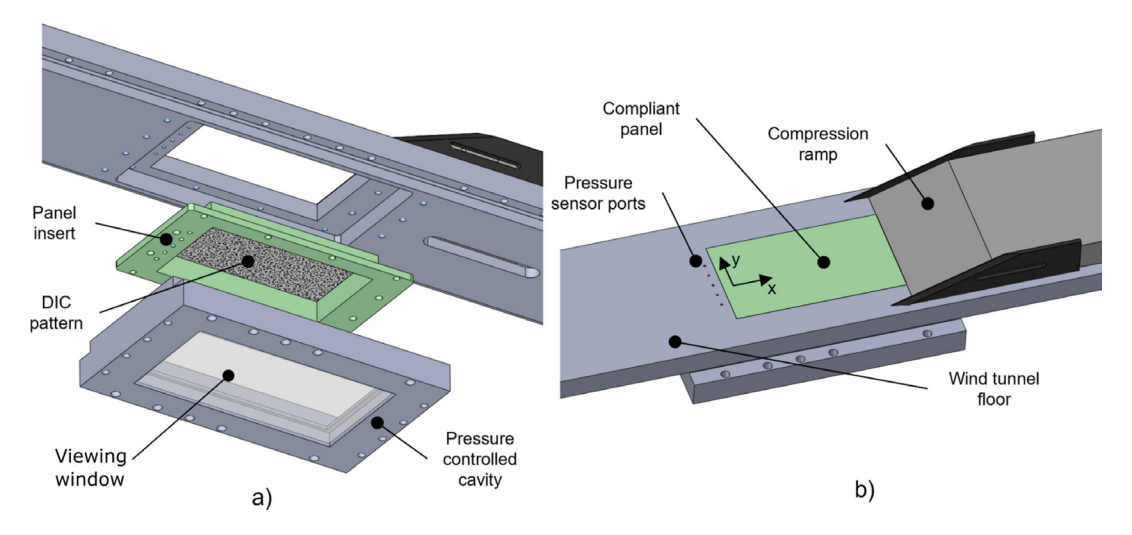


Fig. 4. Panel insert in wind tunnel floor. Lower view (a) with cavity and top view (b) with ramp.

from particle image velocimetry in the test section. The stagnation temperature was measured with a thermocouple in the stagnation chamber. A pressure transducer in the stagnation chamber measured the total pressure.

3.2. Experimental setup

The floor of the wind tunnel test section had a rectangular cutout of width and length 73.7 mm \times 132.1 mm. The compliant panel insert was bolted in the cutout of the wind tunnel floor. Fig. 4 shows the tunnel floor with the panel insert. A rectangular enclosure with a viewing window on the bottom side and open on the top was attached to the lower side of the tunnel, enclosing the compliant panel. The viewing window in the bottom of the cavity was 172.7 mm long, 72.2 mm wide and 9.5 mm thick borosilicate glass that was bonded directly to the metal cavity. The resulting cavity enclosed a volume of 58 cm³ with a depth of 40 mm. A pressure transducer (Baratron 626A, range 0-133 kPa) and a vacuum pump were attached to this cavity through an opening at the side. The vacuum pump was used to reduce the static pressure difference acting on the compliant panels. The control valve for the pump was set to achieve a stable cavity pressure slightly above freestream pressure. During tunnel run this pressure slightly dropped and ended up near freestream pressure. Since the valve was not controlled during the tunnel run, slight variations in the final cavity pressure occurred. There were five small holes in the wind tunnel floor section just upstream of the panel along the spanwise direction. These connected the tunnel test section to the cavity and could be used to insert Kulite pressure transducers. In most test cases, the center hole was filled with a pressure transducer and the remaining ones were plugged, so that no airflow occurred between cavity and test section. A 20° compression ramp was positioned just downstream of the panel insert. The width of the ramp was slightly more than the width of the panel insert, but less than the test section. Fences of height 12 mm were fixed to the sides of the ramp in the streamwise direction to reduce cross-stream flow over the sides of the ramp.

The full experimental setup is depicted in Fig. 5. Two cameras were set up below the tunnel at a slight relative angle viewing the lower side of the panel. They were spaced approximately 46 cm apart from each other at a distance of 81 cm below the panel. This stereoscopic setup was used to measure the panel deformation with 3D-DIC. An LED array placed in-between the cameras illuminated the speckle pattern to ensure sufficient contrast in the images. Details regarding the DIC setup are provided in Section 3.3. Just above the tunnel test section, a third camera was installed that viewed the flow-facing side of the panel through a window installed in the tunnel ceiling. This camera was used to measure the surface pressure on the panel with PSP. An additional LED located above the tunnel served to illuminate the PSP. Details regarding the PSP setup are provided in Section 3.4.

During a wind tunnel run, four data-acquisition systems were running simultaneously. The PSP system measured the surface pressure, the DIC system measured the panel deformation, a Kulite pressure transducer measured the free stream pressure p_{∞} upstream of the panel and an additional transducer measured the pressure p_c within the cavity. Two separate computers were used in this setup. PC-1 ran the software (Davis 10.1 by LaVision) that controlled the cameras used for DIC (hereafter referred to as the DIC cameras). PC-2 ran the software (Photron PFV4) to control the camera above the tunnel (hereafter referred to as the PSP camera). To initiate a measurement, a TTL trigger signal was generated by the PFV4 program on a user command and sent from the computer (PC-2) to the PSP camera, which then started recording. The trigger signal was sent to a timing unit (LaVision portable timing unit (PTU)) that controlled the cameras located below the tunnel. Similar to the trigger signal, the 50 kHz clock signal on which the PSP camera ran (it recorded at

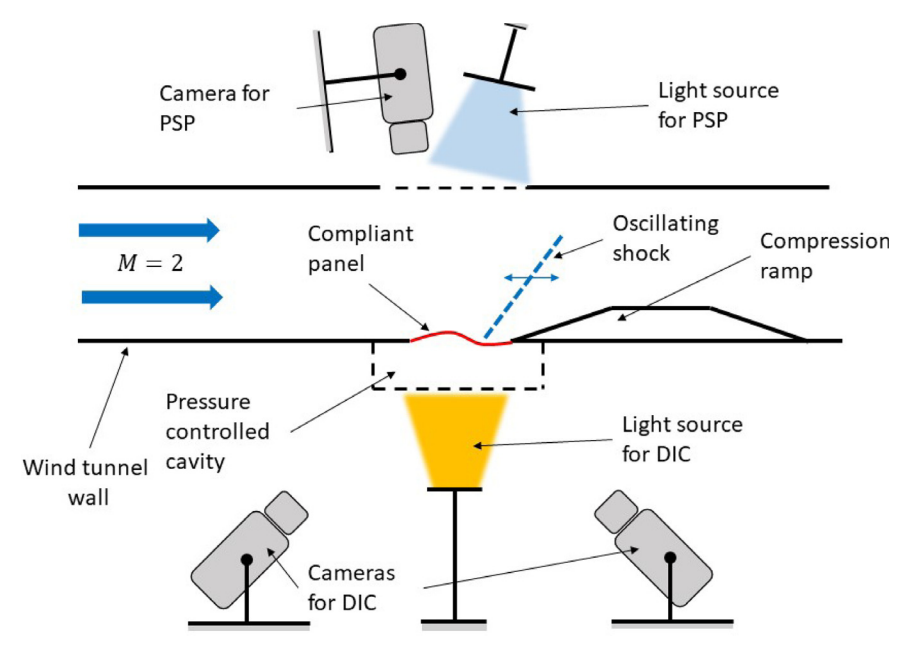


Fig. 5. Full experimental setup at wind tunnel.

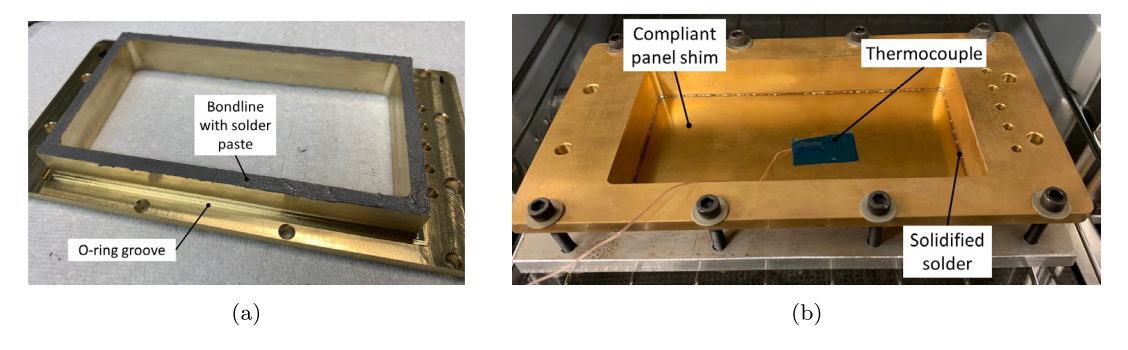


Fig. 6. Reflow soldering process of panel, (a) solder paste on base, (b) sandwiched panel insert in oven with thermocouple.

 $f_s = 50\,000$ frames per second), was forwarded to the PTU. The DIC cameras recorded only at $f_s = 5$ kHz and thus the original clock signal was first down sampled. This was done using two timing boxes (Stanford Research Systems, DG535) that converted the high-frequency signal to a synchronized low-frequency signal. The trigger signal which started the recording of all three cameras was also sent to a data acquisition system (cDAQ by National Instruments, connected to PC-1). The cavity pressure sensor was attached to this cDAQ. Similarly, the Kulite pressure transducer was sampled at 100 kHz and connected to a separate data acquisition system (PXIe by National Instruments, connected to PC-2).

A set of four compliant panels was fabricated, varying in thickness (h = 0.508 mm, 0.406 mm, 0.305 mm and 0.254 mm). Each panel was made from 260 brass shim stock of length and width 121.9 mm and 63.5 mm respectively. Each shim was bonded to a brass base, to form a single panel insert, that could be bolted into the tunnel test section. The base contained a 5.1 mm wide ledge on which solder paste was applied, see Fig. 6(a). The shim was then pressed onto the base and heated in a small oven until the solder melted and bonded the panel to the insert, see Fig. 6(b). The bondline proved strong enough to withstand static shear and vibratory loads during all wind tunnel runs and no failure was observed.

3.3. High-speed digital image correlation (DIC)

Two monochromatic high-speed cameras (Phantom Miro M310) were used to measure structural deformation of the panel. Each camera was equipped with a Scheimpflug adapter as well as a 105 mm Nikon lens with an f-stop setting of 5.6. The cameras were controlled using the software Davis 10.1 by LaVision, which performed synchronization of the

cameras, calibration as well as the DIC computation in post-processing. A speckle pattern was created by using the open-source Python code "speckle_pattern.py" from the Laboratory for Dynamics of Machines and Structures at the University of Ljubljana, Slovenia. The speckle pattern was custom-made for the specific camera setup to result in randomly distributed speckles with diameters not exceeding seven pixels. The pattern was printed onto thin adhesive paper (AVERY address label, thickness 0.14 mm) and attached to the DIC side of the panel.

The stereoscopic DIC system was calibrated using the Davis calibration routine. A calibration pattern was printed and glued onto a flat surface and images were taken at nine different out-of-plane locations, spaced 0.5 mm apart. The resulting pixel resolution after calibration was 6.9 px/mm. To determine a noise floor, a set of 100 images was recorded of the motionless panel. The temporal standard deviation of the noise floor for the out-of-plane deformation was approximately 3 μ m for most of the panel area. The sampling frequency was set to $f_s=5000\,$ Hz with an exposure time of 100 μ s. Data was recorded for a duration of 2 s once steady flow conditions were observed. An LED array was used in continuous mode to illuminate the speckle pattern. The DIC results were validated locally with a Laser-Doppler-Vibrometer, details of this can be found in Appendix C.

3.4. High-speed pressure sensitive paint (PSP)

Polymer/ceramic pressure sensitive paint was used to obtain fast response, full field surface pressure data (Egami et al., 2020). The paint is based on the luminophore ruthenium whose emission of light is quenched by oxygen, thus allowing its use for pressure sensing applications. The polymer/ceramic PSP was mixed on location and sprayed directly onto the flow-facing side of the panel using a spray gun (Paasche Airbrush H0318). The binder consisted of a mixture of silicone and TiO₂ particles. The mixing and painting was done on the day prior to each experiment. During the wind-tunnel run, a custom-built blue LED light (peak wavelength at 460 nm) excited the paint. Its design was based on the CBT-120 LED chip by Luminus. The light was operated in continuous mode for the entire duration (\approx 2 s) of the image acquisition time. Images of the PSP were recorded using a Photron Mini Fastcam AX50. A 35 mm focal length Nikon lens was used with an f-stop value of 2. The frame rate was set to $f_s = 50$ kHz with an exposure time of 10 μ s. The frame rate was set higher than the maximum frequency response of the PSP (around 20 kHz) to reduce aliasing effects. This setup generally leads to acceptable results up to at least 10 kHz (Musta et al., 2021). PSP data was spatially averaged over an area equivalent to the size of an XCQ-062 Kulite transducer, approximately 7×7 px² $\approx 2.5 \times 2.5$ mm², whenever single pressure values were extracted, such as for in-situ calibration on the rigid panel.

4. Results and discussion

Multiple tests were performed to characterize the behavior of the panels in the absence of aerodynamic effects. This information is useful when interpreting the results obtained during the tunnel runs and is a necessary step in the quality control process of each panel. This data is further critical for updating numerical models. While the simulation of the panel vibrations in the wind tunnel is not within the scope of this paper, some of the pre-tests are still provided in this section to help the reader understand the behavior of the panels. The results of static deformation tests, as well as modal analysis of the loaded panels can be found in the Appendix.

4.1. Effect of DIC sticker and PSP on modal parameters

Test were performed to evaluate the influence of the DIC sticker on the vibratory behavior of the thin brass panels. Investigations showed no measurable effect on stiffness but up to 20% increase in damping ratio. This was likely higher than if paint had been used to create the speckle pattern. However it was judged that the advantage of having perfectly repeatable patterns for all panels outweighed the large increase in damping.

4.2. Thermoelastic stiffening

As discussed previously, thermal effects can play a major role in the dynamic behavior of the panels. The total temperature of the air decreased during the tunnel run due to the expansion of the flow in the high-pressure tanks and through the control valve. The cooler air that entered the test section cooled the thin brass panel faster than the steel wind tunnel walls and thus in-plane tensile stresses were produced.

The cooling of the panel can be estimated by computing the recovery temperature of the flow. In theory, once steadystate conditions for the flow and the temperature are reached, the tunnel wall and thus the panels should approximately be at the adiabatic wall temperature, which is the recovery temperature of the flow. For a turbulent boundary layer, the recovery temperature can be written as

$$T_r = T_\infty \left(1 + r \frac{\gamma - 1}{2} M_\infty^2 \right),\tag{3}$$

where $\gamma = 1.4$, $M_{\infty} = 2$ and the recovery factor r is the cubic root of the Prandtl number for a turbulent boundary layer. For the given flow conditions the recovery temperature is approximately 272 K. The panels are expected to eventually cool

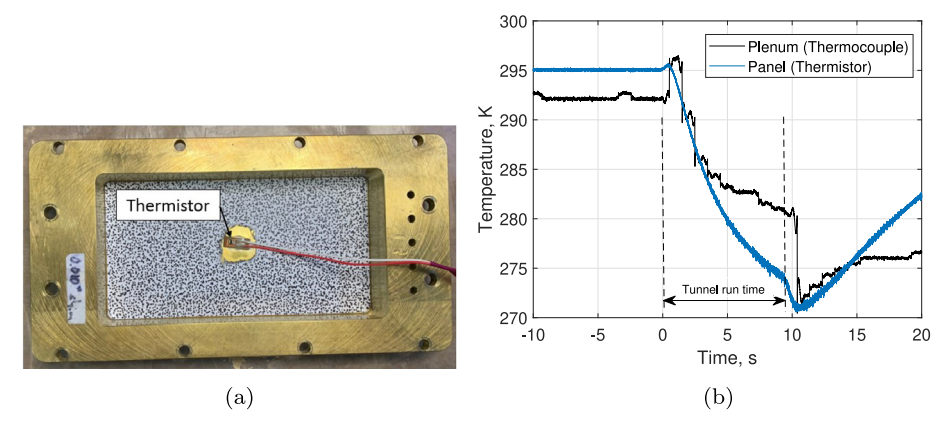


Fig. 7. Temperature measurements during tunnel run; (a) thermistor setup, (b) measurement result.

to that temperature when the adiabatic flow condition is reached. Technically there will always be some heat transfer between the ambient air in the cavity through the panel and into the flow. However, the heat transfer between the turbulent boundary layer and the upper side of the panel is orders of magnitude faster than the heat transfer between the lower side of the panel (with the DIC sticker attached) and the still air in the cavity. Thus the approximation of an adiabatic condition is reasonable.

An experiment was performed to measure the cooling of the panel. A thin film thermistor (OMEGA TFPS-TH-TF-T-40, size $5 \times 10 \times 0.25$ mm) was used to measure the panel temperature during a run. Using thermally conductive silver epoxy, the sensor was glued directly to the thinnest panel near its center, where a small piece of the DIC sticker was removed, see Fig. 7(a). The time history of the panel temperature is shown in Fig. 7(b), along with the stagnation chamber (plenum) temperature. It can be seen that the panel cooled down to about 274 K before the tunnel was shut down. The results shown are for a test in which the ramp was installed. The temperature measurements were repeated for the same panel without the ramp and no significant difference in the temperature drop was measured. Thus thermal effects were not further considered when analyzing the effect of the SBLI, since the conditions remained sufficiently similar in-between the tests with and without ramp. Note that these tests were performed at the end of the test campaign, meaning the added weight of the thermistor did not influence the vibration results discussed in the following section. To account for the transient cooling after the tunnel start, all measurements were performed approximately six seconds after tunnel start to minimize panel temperature differences in-between tunnel runs. Detailed calculations of the thermally induced in-plane stresses require knowledge of the full temperature field. In this study however, no measurement hardware was available to perform these measurements, such as thermal cameras or temperature sensitive paint. To better understand the temperature distribution of a thin panel, the interested reader is referred to the study by Gramola et al. (2021). They performed detailed modeling of the temperature field in a similar experiment and evaluated its effect on surface pressure measurements from PSP.

4.3. Effect of ramp on panel response

4.3.1. Analysis of deformation power spectra

Shown in Fig. 8 are deformation power spectra of a single point on each of the four panels. The point location is at x=90 mm, y=-10 mm and was chosen to avoid nodal points of the lower panel modes. This point is labeled as reference point 'B' in Fig. 8(a). The power spectra are computed using Welch's method, which reduces the noise in power spectral density by averaging windowed subsets of a time history. The total number of 10 000 data points (two seconds recorded at $f_s=5$ kHz) is divided into subsets of length 1000 with an overlap of 500 data points and multiplied with a Hamming window. The frequency content below 200 Hz is not plotted since that region is well below the fundamental frequency for all panels. Each plot shows the comparison between two successive runs, one without the ramp and one with the ramp installed. The measured pressure difference ΔP is listed for each case. While these values differ between test runs of different panels, they were attempted to vary only slightly in between the two consecutive tests performed on the same panel (with and without ramp). Since no parameters apart from the ramp were changed in between these two runs, the difference in response should be only due to the effects of the ramp-induced SBLI.

The response of each panel in the presence of supersonic flow, both without and with an SBLI present, contains multiple structural modes as can be seen by the distinct peaks in the power spectra. The response for both cases is dominated by the first mode, which is the largest peak in each spectrum. For all panels, the presence of SBLI does not modify the amplitude of the first mode beyond what occurs for the supersonic turbulent boundary layer alone; both amplitude and frequency remain mostly constant. However, the higher modes and especially the second mode (second lowest frequency peak) are clearly affected by the presence of the SBLI. The inclusion of the ramp significantly increases the amplitude of vibration of

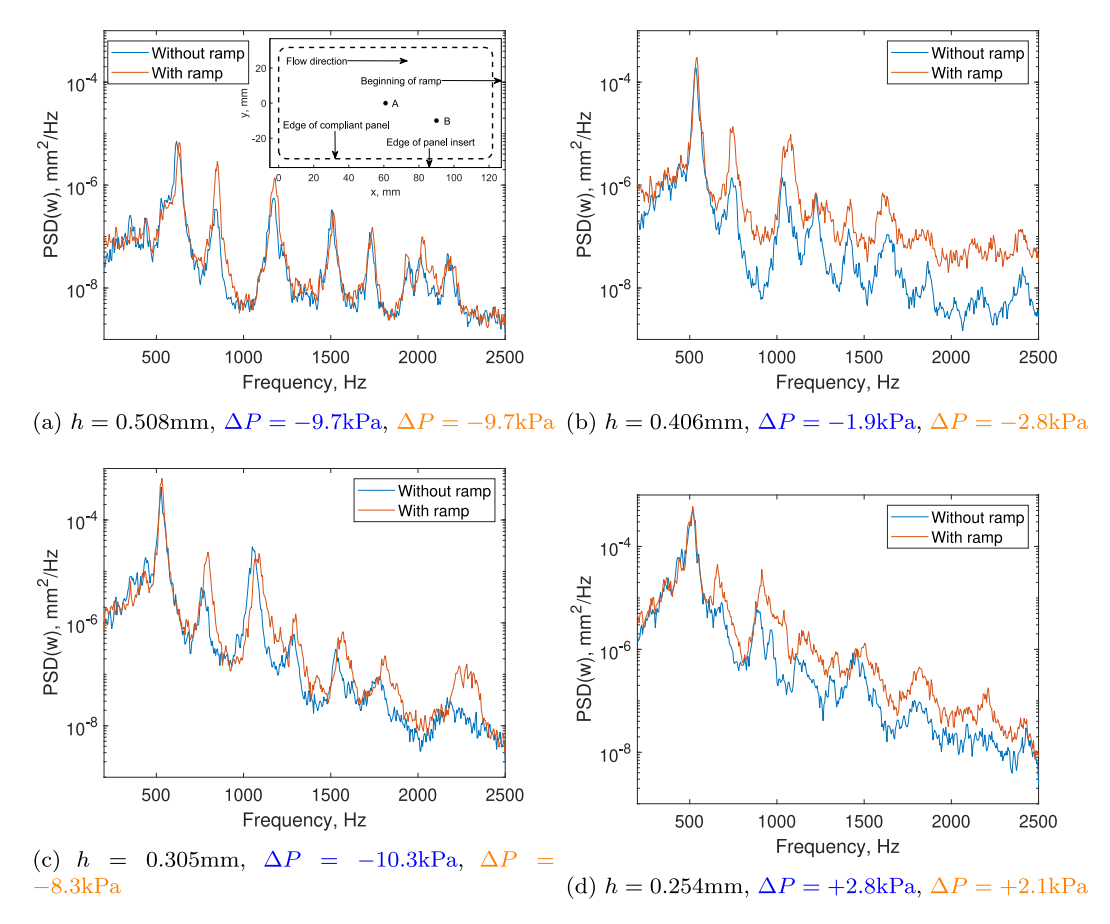


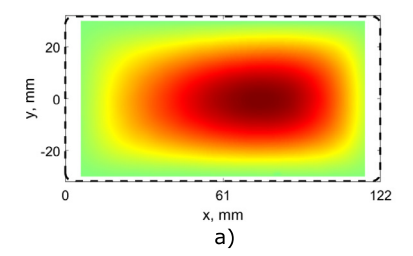
Fig. 8. Deformation power spectra at reference point 'B' from DIC, (a) h = 0.508 mm, (b) h = 0.406 mm, (c) h = 0.305 mm, (d) h = 0.254 mm.

the second mode, this can be seen in all test cases. A likely explanation for this higher mode behavior is localized forcing by the unsteady shock foot, which preferentially excites the second mode and presumably higher ones also. Fig. 3(b) shows the standard deviation of the pressure field for a rigid panel case with ramp. The shock foot intermittent region is characterized by large pressure fluctuations due to shock motion, which leads to large forcing on the structure. The second panel mode consists of a nodal line near x = 66 mm with two asymmetric peaks, one downstream and one upstream. A simulation result of this mode is shown in Fig. 1. The large pressure fluctuation region is located near the downstream peak of that vibration mode and thus primarily excites it through localized forcing. Note that the plots generally also show an increase in vibration of higher modes due to the SBLI, though it is not as prominent and consistent as for the second mode.

4.3.2. Operational modal analysis

The power spectra of the previous section show that the ramp-induced SBLI increases panel vibration of the second structural mode. Most of the vibrational energy in the system however is contained in the fundamental mode. The local power spectra indicate that SBLI has virtually no effect on the fundamental mode vibration, neither in frequency nor amplitude. This is made clear by analyzing the behavior of the first bending mode. Using a system identification algorithm known as complexity pursuit (CP) developed by Stone (2001), the dynamic response of the panel measured with DIC during the tunnel runs can be decomposed into its modes. Shown in Fig. 9 are the operational deflection shapes for the thinnest panel with and without SBLI, corresponding to the first frequency peak. The ODS on the left represents a test case without the compression ramp and the column on the right shows test cases with the compression ramp (and thus with SBLI).

By looking only at the left ODS (test case without the ramp) the it seems to be skewed in the downstream direction (to the right). This is evidence of fluid–structure coupling (panel motion couples with attached flow) and the direction of the skew is based on the flow direction. This effect was previously discussed in Section 2, and visualized in Fig. 1. This skewing effect is much less pronounced in the thicker panels, where structural stiffness dominates the aerodynamic stiffness and is thus not shown here.



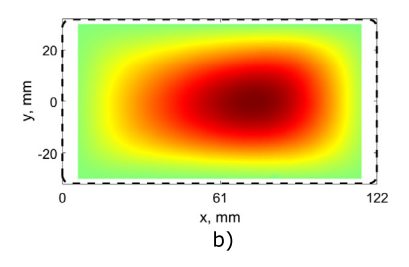


Fig. 9. First ODS for test case without ramp (a) and with ramp (b); flow from left to right; ramp located at x = 127 mm.

A second conclusion that follows from these results is that the SBLI has essentially no effect on the first mode shape/ODS. This can be seen by comparing the ODS on the left and right. Qualitatively, they seem fairly similar, though upon close visual inspection, small differences can be seen between the two. A quantitative comparison between two ODS is made by computing the modal assurance criterion (MAC). The MAC represents the cosine of the angle between the two shape vectors. A MAC value of zero means that the shapes are orthogonal to each other and a value of unity means that they are identical (or rather parallel). The MAC value for these two shapes is greater than 0.995, thus they are essentially identical. This is an interesting result and not intuitive. It means that even though the flow field changes due to the SBLI, there is no coupling mechanism that results in changes to the first mode behavior of the panel, at least for the given flow and geometric conditions. This similarity was observed for all of the thicker panels as well, where MAC values of greater than 0.995 were computed.

4.4. Correlation between pressure and deformation

The previous section only discussed the structural response of the panel. This section now takes into account the pressure field that was measured with PSP. Based on piston theory, which was discussed in Section 2, a surface pressure change is locally related to the streamwise slope and out-of-plane velocity of the panel, whereby the influence of the slope dominates at low frequencies. In the following discussion, the relation between local deformation gradient and surface pressure is investigated. A full-field analysis is performed, where the time-histories of the pressure and deformation are first band-pass filtered and then conditionally averaged. In short, the deformation distribution is recorded at each time step and the streamwise gradient is computed and used in first order piston theory to predict surface pressure distribution. The goal of this analysis is to demonstrate the validity of the piston theory for a test case without ramp and thus show the presence of fluid–structure coupling.

The full field analysis is based on conditional averaging and contains multiple steps. These steps are:

- 1. The natural frequency of a structural mode is identified by analyzing the power spectrum of the deformation at a single point on the panel.
- 2. A high-order temporal band-pass filter centered at the natural frequency (7th order Butterworth filter, bandwidth 40 Hz) is applied to the deformation time histories (from DIC) and the surface pressure time-histories (from PSP) of each point on the panel.
- 3. The deformation time history (after filtering) of a single point on the panel (e.g. at the center) is plotted. The 100 largest peaks and the time instances corresponding to those peaks are identified and stored.
- 4. Surface plots are created of the (previously band-pass filtered) deformation at each of these 100 time steps. These surface plots are averaged to obtain one single surface plot, which shows the deformation amplitude of the band-pass filtered data.
- 5. Surface plots are created of the (previously band-pass filtered) surface pressure at the same 100 time steps at which the deformation showed a peak. These surface plots are averaged to obtain one single surface plot, which shows the surface pressure amplitude of the band-pass filtered data.

The analysis is performed for the thinnest panel (h = 0.254 mm) for the first two modes. The results are plotted in Fig. 10. There is reasonable agreement between the measured pressure field, and the piston theory prediction (second and third row). The overall structure of the pressure field is well predicted but there are significant discrepancies near the edges of the panel. These arise likely from errors in the PSP, resulting for example from temperature effects (Gramola et al., 2021). Based on temperature measurements made at the center of the panel, the temperature difference could be as large as 20 ° K between the center and panel edge, which could cause a bias error in pressure of up to 30%. This temperature-induced error would affect the pressure field but not the frequency content of the pressure fluctuations. On the whole, however, the agreement seems sufficient to clearly show the presence of fluid–structure coupling between panel and supersonic flow in the case without compression ramp. Similar results were obtained for test cases with the ramp, with the discerning difference that the pressure fields only agreed upstream of the SBLI region (x < 100 mm), since the piston theory is not applicable in the separated flow region.

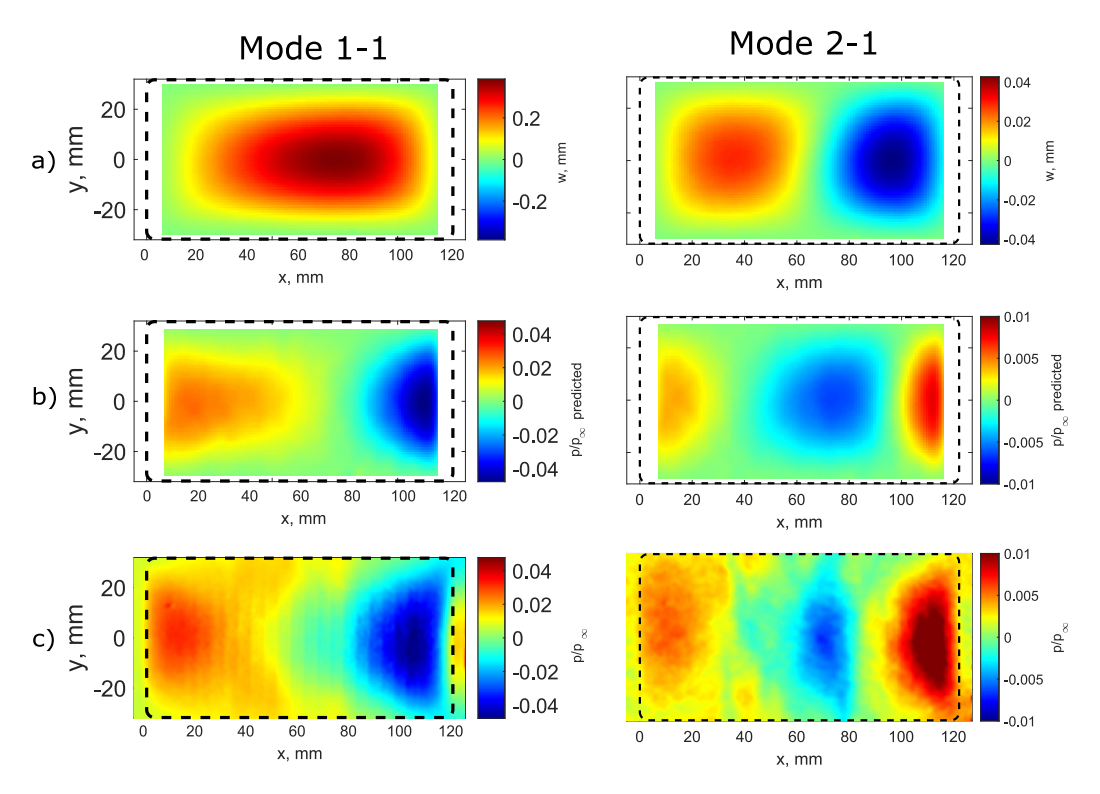


Fig. 10. Full field comparison of band-pass filtered deformation and pressure field (h = 0.254 mm) for two modes. (a) Deformation from DIC, (b) predicted pressure field from piston theory based on wall angle, (c) measured pressure from PSP; flow from left to right.

4.5. Shock foot motion

The analysis so far has focused mostly on how the surface pressure field is affected by the structural vibrations. These surface pressure oscillations are local effects that might not be of importance to other parts of a flight vehicle. In contrast, the motion of the shock can have a large influence on other surfaces on which it impinges. The motion of the shock foot is discussed, based on measurements from PSP.

The nature of the surface pressure and the inferred separation shock foot motion was already discussed in Section 2 for a rigid panel. This section will now highlight the effect of structural compliance on the shock foot motion as well as provide some more details regarding its computation. Similar to previous studies of unsteady SBLI (Erengil and Dolling, 1991), the shock foot, hereafter referred to as SF, is defined based on a surface pressure threshold value. In the present study, the pressure threshold value is defined separately for each test based on visual inspection of the surface pressure data from PSP, typically around 1.2 similar to Babinsky and Harvey (2014). The shock foot position is then estimated using an algorithm consisting of several steps. First, the pressure field obtained from PSP is binarized, meaning each pixel either is assigned a value of zero or one, based on the user-defined pressure threshold. A set of interpolations is performed next, which fill small voids in the high and low pressure regions. The algorithm then obtains the edge between the two regions and stores the location of that line as a single vector. This process is then repeated for all time steps. The computation is based on functions available in the MATLAB image processing toolbox; a computationally inexpensive process, which can be performed within seconds for thousands of images on a regular desktop computer.

The power spectral densities of the shock foot motion x_{SF} at the panel centerline are computed for each panel and are shown in Fig. 11. In each plot, the frequencies of the first three panel bending modes are shown as vertical dashed lines. The plots show that the shock primarily oscillates at the same frequency as the first mode of the panel. This shock motion becomes larger for the thinner panels, where the vibration amplitudes are also larger. While the shock motion contains multiple peaks that correspond to panel vibration modes (especially higher modes in the case of the thinnest panel), they are about an order of magnitude lower than the first vibration mode.

The analysis performed in previous sections shows that the SBLI does not modify the first mode of the panel, neither its shape nor its frequency or amplitude. This means that while the shock and panel oscillate at the same frequency, it is not two-way coupling. The panel vibration dictates the motion of the shock, but the shock (or rather the SBLI) does not modify the dominant first mode panel vibration.

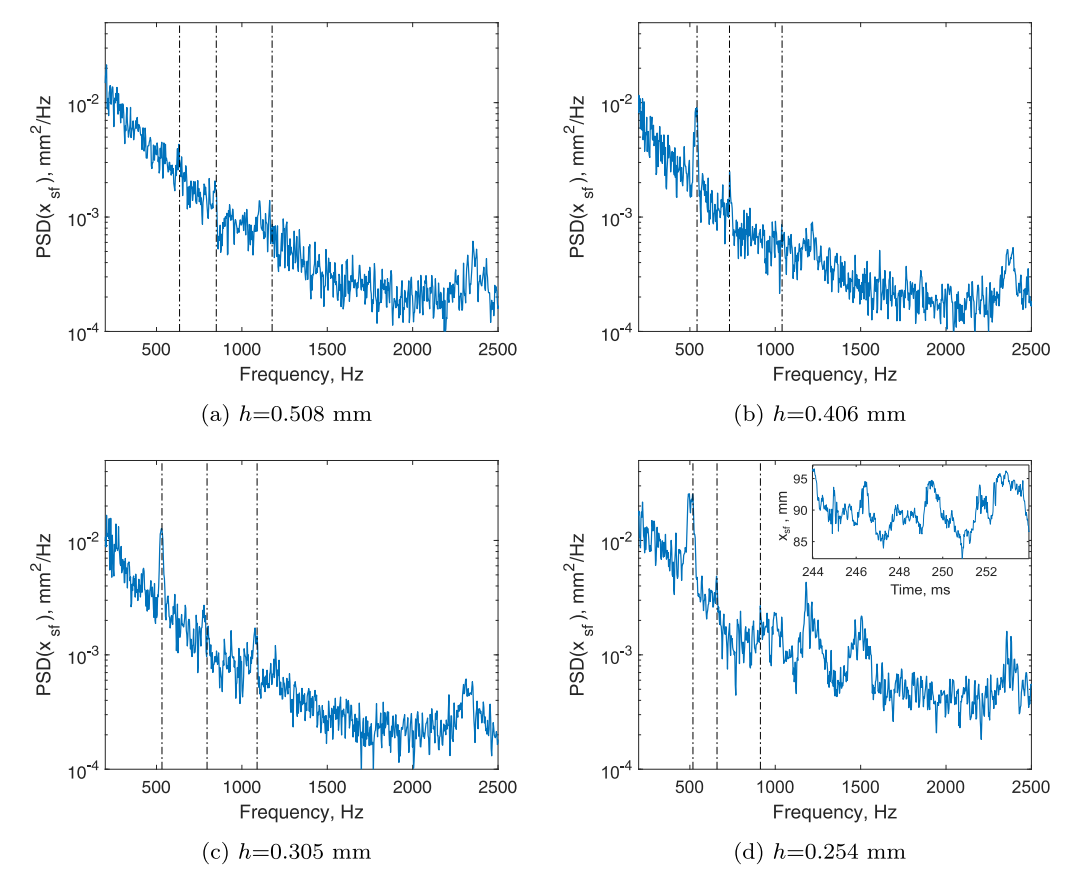


Fig. 11. Motion of shock foot in streamwise direction at centerline. Dotted lines denote first three structural modes.

5. Summary and conclusion

This study investigated the interaction between a Mach 2 flow over a 20° compression ramp and a compliant panel. The goals of this work were to investigate the effect of the ramp-induced SBLI on the dynamics of the system. Panels of different thicknesses were investigated and thinner panels generally showed larger vibration amplitudes and stronger fluid-structure coupling. This was observed both without and with SBLI. High-speed stereoscopic DIC and fast-response PSP were used to obtain time-resolved, synchronous structural deformations and surface pressure fields. Linearized piston theory was used to predict pressure maps based on the local measured wall angle of the deformed panel. The predictions and measurements matched sufficiently well to prove the presence of fluid-structure coupling. This analysis further demonstrated the advantage of time-resolved, synchronous DIC and PSP for the measurement of this type of coupled system. Deformation power spectra showed that the supersonic turbulent boundary layer alone (no SBLI) excited the structural bending modes of the panel. The SBLI primarily increased the vibration amplitude of the higher structural bending modes, without significant effect on the first mode. This was further shown by comparing the first vibration mode shape/ODS for test cases without and with ramp; the operating deflection shapes were modified in a similar way both without and with the presence of an SBLI. While the SBLI did not significantly affect the first panel mode beyond what was observed for the supersonic boundary layer alone, the first panel mode did affect the unsteadiness of the SBLI. This was shown by analyzing the motion of the shock foot using surface pressure data from pressure sensitive paint, which oscillates primarily at the fundamental structural mode frequency. The argument that the shock oscillation is dictated by the fundamental panel vibration is based on inferring shock motion from PSP. The data collected in this work supports this one-sided relation. The results presented in this paper indicated that for the given flow conditions and choice of structural parameters, the dominant dynamics of the fluid-structure system remained mostly unaffected by the presence of ramp-induced SBLI. This result is likely due to the fact that the majority of the panel surface is governed by piston theory and only a small part near the ramp is influenced by the SBLI. For larger ramp angles which increase the size of the separation region this will likely not be the case. Results also showed the effect of SBLI on the vibration of higher modes, such as some changes in natural frequency and vibration amplitudes. More detailed analysis of the effect of SBLI on higher structural modes, and their operating deflection shapes are subjects of future investigations. A more detailed measurement of the panel surface temperature is further needed to evaluate the effect on in-plane tension and changes to the PSP response.

CRediT authorship contribution statement

Marc A. Eitner: Formal analysis, Data curation, Visualization, Writing – original draft. **Yoo-Jin Ahn:** Data curation, Formal analysis. **Mustafa N. Musta:** Data curation. **Noel T. Clemens:** Methodology, Project administration, Supervision, Writing – review & editing. **Jayant Sirohi:** Methodology, Supervision, Writing – review & editing.

Declaration of competing interest

The authors declare the following financial interests/personal relationships which may be considered as potential competing interests: Marc Eitner, Yoo-Jin Ahn, Mustafa Musta, Noel Clemens, Jayant Sirohi reports financial support was provided by National Science Foundation.

Data availability

Data will be made available on request

Acknowledgments

This work was supported by the National Science Foundation under award # 1913587. The authors would like to thank Jeremy Jagodzinski for assisting with the measurements.

Appendix A. Natural frequency of loaded panels

As was discussed in Section 2, the presence of in-plane stresses modifies the bending stiffness of a panel and thus changes its natural frequencies. The presence of in-plane stresses in the panels was experimentally determined through

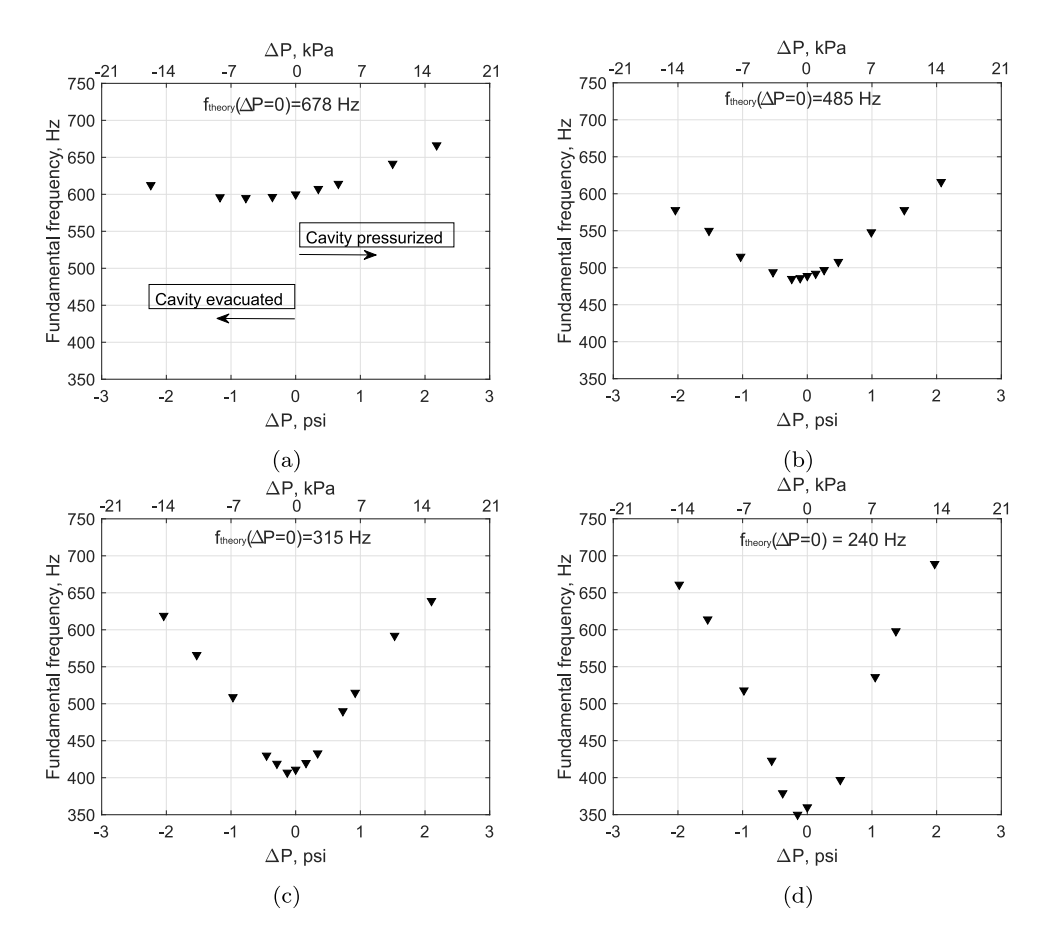


Fig. A.12. Effect of static pressure difference on fundamental frequency, (a) h = 0.508 mm, (b) h = 406 mm, (c) h = 0.305 mm, (d) h = 0.254 mm.

impact testing. All tests were performed with the panel installed in the wind tunnel. The effect of static pressure loading on the first natural frequency of each panel was determined experimentally as well. Using both a vacuum pump and a compressor, the pressure was modified in the cavity resulting in a bulging of the panel into and out of the test section. The panel was directly impacted near its corner using an impact hammer and the response was measured with a capacitive displacement sensor located near (but not exactly at) the center. An average of three impacts was taken to compute the FRF at each pressure value and the first natural frequency was calculated. The resulting plots for the four panels are shown in Fig. A.12. The curves have the same shape as the simulated data shown previously in Fig. 2. The lowest frequency value in all cases is slightly off-center, which is likely the result of the panels not being perfectly flat during fabrication. The importance of these tests can be seen by comparing the measured natural frequencies at zero pressure loading to the values predicted by the numerical model described in Section 2. Updating of the in-plane boundary stiffness and including external in-plane loads is necessary to match the experimental data to the numerical model for each panel separately. To ensure no change in boundary conditions (e.g. from bolt tension), the panels were never removed from the tunnel once installed and only removed once all tests were performed.

Appendix B. Static deformation of loaded panels

The out-of-plane deformation of each panel was measured while a static pressure difference was applied. This data is provided here to further aid in updating a structural model (see Fig. B.13).

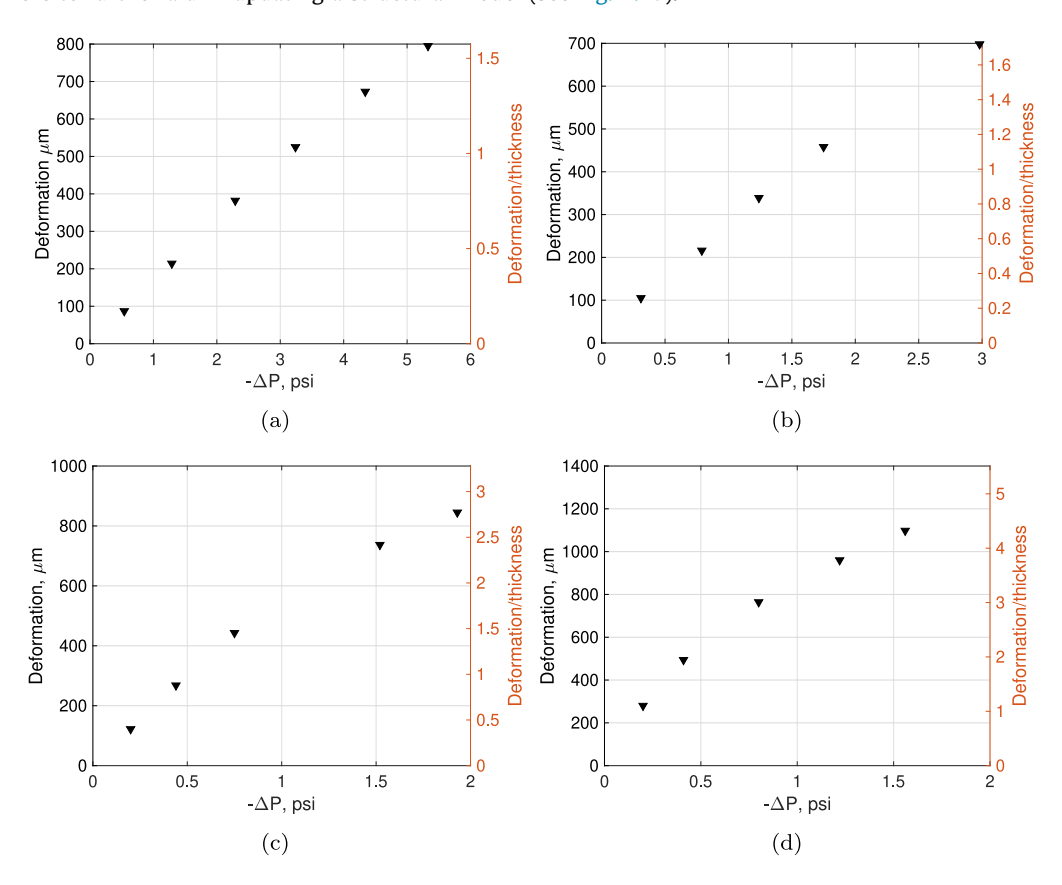


Fig. B.13. Static deformation of panels at center under uniform pressure loading, (a) h = 0.508 mm, (b) h = 0.406 mm, (c) h = 0.305 mm, (d) h = 0.254 mm.

Appendix C. DIC validation

The out-of-plane deformation measured with DIC was compared to the measurements from a Laser-Doppler-Vibrometer (Polytec Vibroflex-QTec). Shown in Fig. C.14 are the power spectral densities of the vibration at the center of a thin steel panel (not discussed in this work) during tunnel operation. There is excellent agreement, with small discrepancies at very low frequencies (below 100 Hz) that originate from camera vibration.

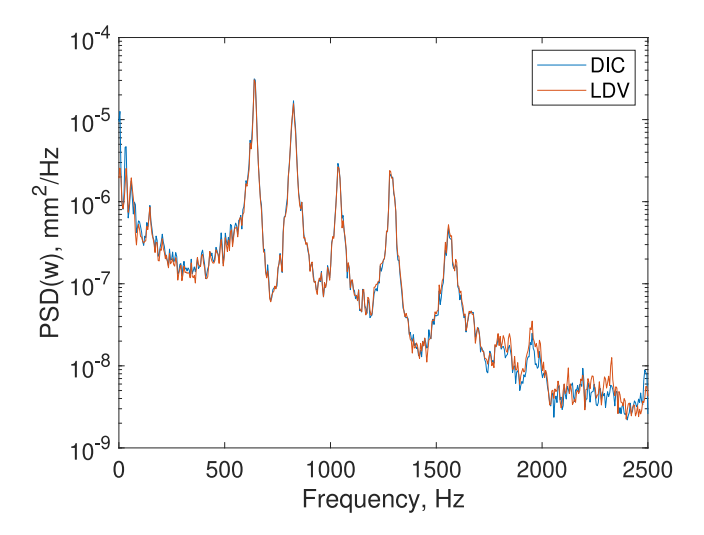


Fig. C.14. Validation of DIC results with LDV.

References

Ahn, Y.-J., Eitner, M., Rafati, S., Musta, M., Sirohi, J., Clemens, N., 2022. Experimental investigation of fluid-structure interaction in mach 2 flow using simultaneous high-speed piv and dic, 20th International Symposium on Application of Laser and Imaging Techniques to Fluid Mechanics. URL https://par.nsf.gov/biblio/10357649.

Babinsky, H., Harvey, J.K., 2014. Shock Wave-Boundary-Layer Interactions, first ed. In: Cambridge Aerospace Series, Cambridge University Press, ISBN: 1107646537.

Brouwer, K.R., Gogulapati, A., McNamara, J.J., 2017. Interplay of surface deformation and shock-induced separation in shock/boundary layer interactions. http://dx.doi.org/10.2514/6.2017-0177, AIAA Paper 2017-0177, AIAA Scitech Forum.

Casper, K.M., Beresh, S.J., Henfling, J.F., Spillers, R.W., Hunter, P., Spitzer, S., 2019. Hypersonic fluid-structure interactions due to intermittent turbulent spots on a slender cone. AIAA J. 57 (2), 749–759. http://dx.doi.org/10.2514/1.j057374.

Currao, G.M., Neely, A.J., Buttsworth, D.R., Gai, S.L., 2017. Hypersonic fluid-structure interaction on a cantilevered plate. EUCASS 12, 13.

Dolling, D., Or, C.T., 1985. Unsteadiness of the shock wave structure in attached and separated compression ramp flows. Exp. Fluids 3, 24–32. http://dx.doi.org/10.2514/6.1983-1715.

Dowell, E.H., 1970. Panel flutter - A review of the aeroelastic stability of plates and shells. AIAA J. 8 (3), 385–399. http://dx.doi.org/10.2514/3.5680. Dowell, E.H., 1974. Aeroelasticity of Plates and Shells. vol. 1, Springer Science & Business Media.

Egami, Y., Hasegawa, A., Matsuda, Y., Ikami, T., Nagai, H., 2020. Ruthenium-based fast-responding pressure-sensitive paint for measuring small pressure fluctuation in low-speed flow field. Meas. Sci. Technol. 32 (2), 024003.

Eitner, M.A., Ahn, Y.-J., Musta, M.N., Sirohi, J., Clemens, N.T., 2022. Effect of structural modifications on vibratory response of panel under ramp-induced shock wave boundary layer interaction. http://dx.doi.org/10.2514/6.2022-2486, AIAA Paper 2022-2486, SCITECH 2022 Forum.

Erengil, M.E., Dolling, D.S., 1991. Unsteady wave structure near separation in a mach 5 compression ramp interaction. AIAA J. 29 (5), 728-735. http://dx.doi.org/10.2514/3.10647.

Frendi, A., 1997. Coupling between a supersonic turbulent boundary layer and a flexible structure. AIAA J. 35 (1), 58–66. http://dx.doi.org/10.2514/2.87. Freydin, M., Dowell, E.H., 2021. Nonlinear theoretical aeroelastic model of a plate: Free to fixed in-plane boundaries. AIAA J. 59 (2), 658–672. http://dx.doi.org/10.2514/1.J059551.

Gramola, M., Bruce, P.J., Santer, M.J., 2021. Temperature corrected pressure sensitive paint measurements on a flexible surface, http://dx.doi.org/10. 2514/6.2021-0128.

Maestrello, L., Linden, T., 1971. Measurements of the response of a panel excited by shock boundary-layer interaction. J. Sound Vib. (ISSN: 0022-460X) 16 (3), 385–391. http://dx.doi.org/10.1016/0022-460X(71)90594-3.

Mei, C., Abdel-Motagaly, K., Chen, R., 1999. Review of Nonlinear Panel Flutter at Supersonic and Hypersonic Speeds. Appl. Mech. Rev. (ISSN: 0003-6900) 52 (10), 321–332. http://dx.doi.org/10.1115/1.3098919.

Musta, M.N., Vanstone, L., Ahn, Y.-J., Eitner, M., Sirohi, J., Clemens, N., 2021. Investigation of flow-structure coupling for a compliant panel under a shock/boundary-layer interaction using fast-response psp, AIAA paper 2021-2809, AVIATION 2021 FORUM, http://dx.doi.org/10.2514/6.2021-2809. Neet, M.C., Austin, J.M., 2020. Effects of surface compliance on shock boundary layer interaction in the caltech mach 4 ludwieg tube. http://dx.doi.org/10.2514/6.2020-0816, AIAA Paper 2020-0816, AIAA SciTech Forum.

Schöneich, A.G., Whalen, T.J., Laurence, S.J., Sullivan, B.T., Bodony, D.J., Freydin, M., Dowell, E.H., Stacey, L.J., Buck, G.M., 2021. Fluid-thermal-structural interactions in ramp-induced shock-wave boundary-layer interactions at mach 6. http://dx.doi.org/10.2514/6.2021-0912, AIAA Paper 2021-0912, AIAA Scitech Forum.

Spottswood, S.M., Beberniss, T.J., Eason, T.G., Perez, R.A., Donbar, J.M., Ehrhardt, D.A., Riley, Z.B., 2019. Exploring the response of a thin, flexible panel to shock-turbulent boundary-layer interactions. J. Sound Vib. (ISSN: 0022-460X) 443, 74–89. http://dx.doi.org/10.1016/j.jsv.2018.11.035.

Spottswood, S.M., Eason, T., Beberniss, T., 2012. Influence of shock-boundary layer interactions on the dynamic response of a flexible panel. In: Proceedings of the ISMA-2012. pp. 17–19.

Stone, J.V., 2001. Blind source separation using temporal predictability. Neural Comput. 13 (7), 1559–1574. http://dx.doi.org/10.1162/089976601750265009.

Tan, S.S., Bruce, P.J., Gramola, M., 2019. Oblique shockwave boundary layer interaction on a flexible surface. http://dx.doi.org/10.2514/6.2019-0097, AIAA Paper 2019-0097, AIAA Scitech Forum.

Thayer, J.D., McNamara, J.J., Gaitonde, D.V., 2022. Unsteady aerodynamic response of a high-speed, separated flow to a deforming cantilever plate. http://dx.doi.org/10.2514/6.2022-0292, AIAA Paper 2022-0292, Scitech 2022 Forum.

- Tripathi, A., Gustavsson, J., Shoele, K., Kumar, R., 2021. Response of a compliant panel to shock boundary layer interaction at mach 2. http://dx.doi.org/10.2514/6.2021-0489, AIAA Paper 2021-0489, Scitech 2021 Forum.
- Varigonda, S.V., Jenquin, C., Narayanaswamy, V., 2021. Impact of panel vibrations on the dynamic field properties in supersonic flow. http://dx.doi.org/10.2514/6.2021-2926, AIAA Paper 2021-2926, Aviation 2021 Forum.
- Varigonda, S.V., Narayanaswamy, V., 2019. Investigation of shock wave oscillations over a flexible panel in supersonic flows. http://dx.doi.org/10. 2514/6.2019-3543, AIAA Paper 2019-3543, AIAA Aviation Forum.
- Vasconcelos, P.B., McQuellin, L.P., Krishna, T., Neely, A., 2021. Experimental study of hypersonic fluid-structure interactions on an inclined clamped-free-clamped-free compliant panel. http://dx.doi.org/10.2514/6.2021-4232, AIAA Paper 2021-4232, ASCEND 2021.
- Whalen, T.J., Schöneich, A.G., Laurence, S.J., Sullivan, B.T., Bodony, D.J., Freydin, M., Dowell, E.H., Buck, G.M., 2020. Hypersonic fluid-structure interactions in compression corner shock-wave/boundary-layer interaction. AIAA J. 58 (9), 4090-4105. http://dx.doi.org/10.2514/1.j059152.
- Willems, S., Gülhan, A., Esser, B., 2013. Shock induced fluid-structure interaction on a flexible wall in supersonic turbulent flow. In: EUCASS Proceedings Series Advances in AeroSpace Sciences. 5, pp. 285–308. http://dx.doi.org/10.1051/eucass/201305285.